Accuracy and resolution of in vitro imaging based porcine lens volumetric measurements

Mark Wendt[a], Kurt Bockhorst[b], Lin He[a], Adrian Glasser[a],[*]

[a] College of Optometry, University of Houston, 505 J. Davis Armistead Building, Houston, TX 77204, USA
[b] Department of Diagnostic and Interventional Imaging, University of Texas Medical School, Houston, TX, USA

ARTICLE INFO

ABSTRACT

There is considerable interest in determining lens volume in the living eye. Lens volume is of interest to understand accommodative changes in the lens and to size accommodative IOLs (A-IOLs) to fit the capsular bag. Some studies have suggested lens volume change during accommodation. Magnetic Resonance Imaging (MRI) is the only method available to determine lens volume in vivo. MRI is, by its nature, relatively low in temporal and spatial resolution. Therefore analysis often requires determining lens volume from single image slices with relatively low resolution on which only simple image analysis methods can be used and without repeated measures. In this study, 7 T MRI scans encompassing the full lens volume were performed on 19 enucleated pig eyes. The eyes were then dissected to isolate and photograph the lens in profile and the lens volumes were measured empirically using a fluid displacement method. Lens volumes were calculated from two- and three-dimensional (2D and 3D) MR and 2D photographic profile images of the isolated lenses using several different analysis methods. Image based and actual measured lens volumes were compared. The average image-based volume of all lenses varied from the average measured volume of all lenses by 0.6%–6.4% depending on the image analysis method. Image analysis methods that use gradient based edge detection showed higher precision with actual volumes (r^2: 0.957–0.990), while threshold based segmentation had poorer correlations (r^2: 0.759–0.828). The root-mean-square (RMS) difference between image analysis based volumes and fluid displacement measured volumes ranged from 8.51 μl to 25.79 μl. This provides an estimate of the error of previously published methods used to calculate lens volume. Immobilized, enucleated porcine eyes permit improved MR image resolution relative to living eyes and therefore improved image analysis methods to calculate lens volume. The results show that some of the accommodative changes in lens volume reported in the literature are likely below the resolution limits of imaging methods used. MRI, even with detailed image analysis methods used here, is unlikely to achieve the resolution required to accurately size an A-IOL to the capsular bag.

© 2011 Elsevier Ltd. All rights reserved.

1. Introduction

Lens volume has been of interest because as the lens grows throughout life (Augusteyn, 2007; Glasser and Campbell, 1999) lens volume increases with age, lens dimensions, and hence volume, vary between individuals of the same age, and lens volume has been suggested to change during accommodation (Gerometta et al., 2007; Sheppard et al., in press; Strenk et al., 2004). There is also interest in understanding if accommodative intraocular lenses

(A-IOLs) can restore accommodation to the presbyopic eye. Although many A-IOLs are either in clinical use, in clinical trials or undergoing research and development, significant challenges still remain for clinically useful accommodative amplitudes to be achieved. One such remaining challenge for A-IOLs that are to be placed within the capsular bag is matching the size of the A-IOL to the size of the capsular bag. This may be essential for optimizing accommodative performance or for customization to an individual eye. Accurate methods for measuring phakic lens volume are needed.

In vivo measurements of the human lens are limited because of the relative inaccessibility of the lens within the eye. Lens axial thickness is commonly measured using A-scan ultrasound, ultrasound biomicroscopy and partial coherence interferometry. Lens

* Corresponding author. Tel.: +1 713 743 1842; fax: +1 713 743 2053.
  E-mail addresses: mwendt@uh.edu (M. Wendt), Kurt.H.Bockhorst@uth.tmc.edu (K. Bockhorst), lhe5@uh.edu (L. He), aglasser@uh.edu (A. Glasser).

thickness and lens surface curvature have also been measured using Scheimpflug imaging (Dubbelman et al., 2005; Rosales et al., 2006), optical coherence tomography (Baikoff et al., 2004), and phakometry (Atchison et al., 2008; Rosales and Marcos, 2006). However, lens equatorial diameter cannot be measured in vivo with any of these methods. Other than lens volume, lens diameter may be one of the more important lens biometric parameters to know for sizing an A-IOL to the capsular bag. Besides a few studies where lens diameter has been measured in vivo in cases of congenital aniridia, ocular albinism (Wilson, 1997) or in iridectomized monkeys (Glasser et al., 2006; Wendt et al., 2008), the only other method that has been used for in vivo lens equatorial diameter and volume measurements is magnetic resonance imaging (MRI) (Atchison et al., 2008; Jones et al., 2007; Strenk et al., 1999).

MRI has been used to measure age-related changes in lens thickness and lens diameter (Atchison et al., 2008; Jones et al., 2007; Kasthurirangan et al., 2011; Strenk et al., 1999), lens radius of curvature (Atchison et al., 2008; Kasthurirangan et al., 2011), lens cross sectional area (CSA) (Strenk et al., 2004), and ciliary body ring diameter (Kasthurirangan et al., 2011; Strenk et al., 1999, 2006). In these publications, lens biometric measurements were calculated from single central MRI slices with in-plane resolutions between 0.078 and 0.31 mm. MRI measurements of in vivo lens dimensions are limited by several factors. MRI is inherently low in spatial resolution (hundreds of microns) relative to other ocular imaging methods (tens of microns). The time required to capture MRI scans is lengthy (seconds to minutes) relative to other ocular imaging methods (milliseconds). The long imaging time in conjunction with ocular instability due to eye blinks or eye movements adds further inaccuracy to the images captured. Low spatial resolution, high image noise and low image contrast make analysis and measurement of MR images inherently inaccurate compared to other ocular imaging techniques such as OCT with axial resolutions of 6–12 μm and lateral resolutions of 27 μm–60 μm (Borja et al., 2010b; Grulkowski et al., 2009; Marussich et al., 2011; Shen et al., 2010; Uhlhorn et al., 2008). The impracticality of routinely doing repeated measures as is typical with other imaging methods, further limits reliability of MRI measurements. To the knowledge of the authors, repeated MRIs have been done on only a single lens in one MRI study (Sheppard et al., in press). MRI studies have been undertaken to attempt to improve image resolution, shorten imaging time and eliminate artifacts for more accurate MRI measurements of the accommodative structures (Langner et al., 2010; Richdale et al., 2009; Sheppard et al., in press). However, little attention has been given to the image analysis methods employed to quantify the MR images. Although the image resolution may represent the primary limitation in determining lens parameters accurately, the image analysis methods used will also have inherent variability.

Several methods have been used to calculate volume from lens images. These images include single slice MR images, profile photographs of isolated lenses and profile images of lenses in situ in partially dissected eyes. Lens volumes have been calculated using CSA of lens profile photographs by counting pixels and then applying the second Pappus centroid theorem (Gerometta et al., 2007; Kong et al., 2009; Zamudio et al., 2008). Lens CSA has also been calculated from a single central MRI slice (Strenk et al., 2004) or from shadow-photogrammetry by fitting an oblate ellipsoid (Borja et al., 2010a; Rosen et al., 2006), polynomials (Urs et al., 2009), or a 10th-order cosine series function (Urs et al., 2010) to the lens surfaces and integrating to find area and assuming axial symmetry to calculate volume. Two groups have used information from an entire lens MR image stack rather than from only a single slice or profile image to calculate lens volume (Hermans et al., 2009; Sheppard et al., in press).

Many mathematical models have been proposed to fit to lens surface 2D cross section profiles. Volume can then be estimated by assuming rotational symmetry about the anterior–posterior axis, although lens volumes have not been calculated with all the proposed 2D surface models. In human lenses, fourth (Strenk et al., 2004) and tenth (Urs et al., 2009) order polynomials have been applied to the anterior and posterior cross sectional 2D lens surface profiles. Also, a 10th-order cosine series function (Urs et al., 2010) has been applied to the entire lens profile. Aspheric equations were applied to half of human lens cross section 2D profiles rotated about the anterior–posterior axis (Dubbelman and van der Heijde, 2001; Hermans et al., 2009). Reilly and Ravi investigated four possible models from which porcine lens volumes could be calculated, including spherical caps, oblate spheroids, and torispherical domes to be applied to the anterior and posterior lens surfaces (Reilly and Ravi, 2010).

While many lens two-dimensional measurements from MR images such as axial thickness and diameter have been compared to other methods, and several studies have calculated lens volumes, no study has determined how accurately volume can be measured from lens images. The study described here was undertaken to determine resolution with which the volume of pig lenses could be measured from images using several different methods. Three dimensional MR images were obtained from whole enucleated pig eyes. These MR images were made with anisotropic voxels as had been done in most previous MRI studies. Following the MRIs, lenses were extracted from the eyes. Volumes were calculated using different combinations of image pre-processing, segmentation, and volume calculation (Fig. 1) applied to three types of lens images (Fig. 2). These calculated values were compared to direct empirical fluid displacement volumetric measurements of the same extracted lenses.

2. Materials and methods

The coordinate scheme used throughout this manuscript is that the axis passing from the anterior surface to the posterior surface along the optical axis of the lens will be referred to as the z-axis (Fig. 3); a sagittal section of the lens is along the z-y plane; an equatorial section of the lens is along the x-y plane; all 2D lens images were acquired in the x-z plane and slices going into the depth of the stack are along the y-axis.

2.1. Eye preparation

Enucleated eyes from approximately 6 month old pigs were obtained from a supplier (Sioux-Preme Packing, Sioux Center, IA) shipped overnight in saline in insulated boxes with ice packs. Some lenses were rejected either because of damage to the lenses during the experiments or because MR images showed fluid separation of the capsule from the lens. Ultimately, data from nineteen eyes was analyzed. Prior to MRI scans, eyes were pressurized via a needle inserted into the vitreous chamber through the optic nerve which was attached to a hydrostatic column with saline filled to a height of 20.4 cm above the eye which corresponds to 15 mm Hg. For MRI scans, the posterior sclera of the intact eyes was glued with cyanoacrylate to the inside wall a 50 ml conical tube and the tube was then completely filled with room temperature saline without air bubbles. MRI methods are detailed below. Following MRI scans, the eyes were removed from the conical tubes, placed in saline, and dissected to remove the cornea and iris. The partly dissected eyes were removed from the saline, the zonular fibers digested with α-chymotrypsin solution (Sigma, St. Louis, MO), the lens was scooped out of the eye with a plastic spatula peeling the lens from the hyaloid membrane, and the lens returned to a saline filled glass
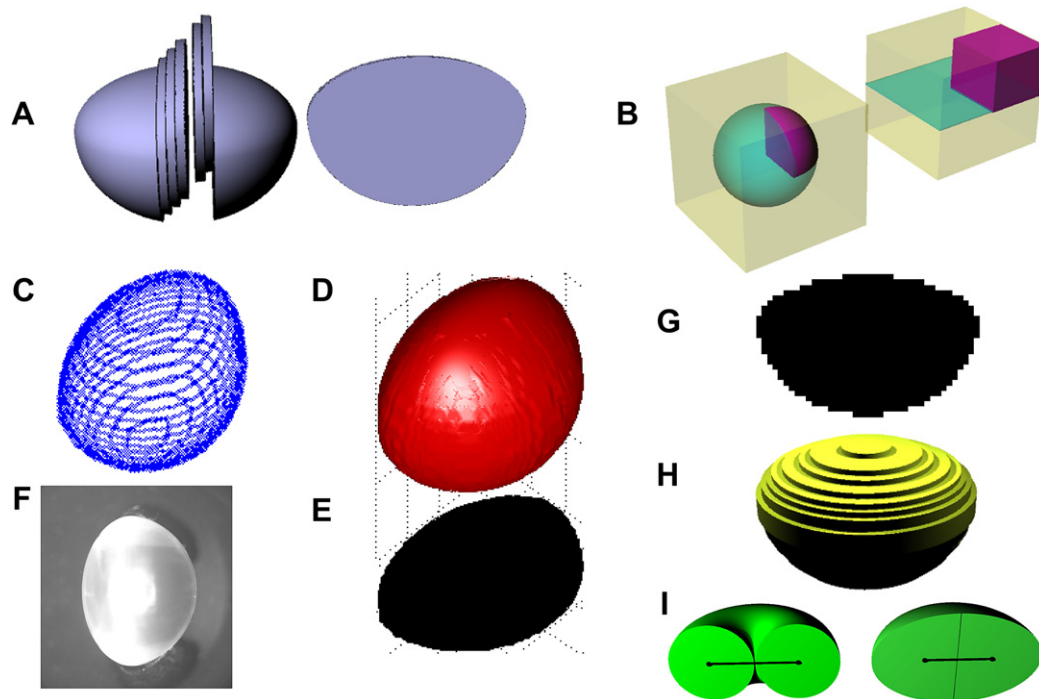
Fig. 1. Pictorial representation of the methods used to analyze the image data. (A) In Methods 2.3.1, several of the near-central slices were examined and volume was calculated from the slice with the greatest cross sectional area. (B) In Method 2.3.2, a spherical transform was performed on the image stack. This diagram shows a sphere (left) and a spherical transform of the sphere (right). The surface of the sphere is shown in green, a segment of the sphere is shown in magenta, and the volume outside of the sphere is shown in yellow. In Methods 2.3.3, (C) the lens edge is segmented in each slice of the image stack, (D) the Cartesian positions of the lens edges are interpolated and a polynomial fit around the edges to outline the entire lens surface, (E) then a 2D projection (black shadow) of the lens is used in Methods 2.3.3.2 and 2.3.3.3. (F) Methods 2.4.1 use a profile image of the lens after the lens has been extracted from the eye. The methods depicted in A, E, and F result in 2D images which are converted to (G) binary images. Volume is calculated from these binary images by two methods: (H) in the sum of disks method, each row of lens pixels in the binary image is assumed to represent a cross section of a disk and the pixels in all disks are summed; (I) using Pappus' Theorem, the volume is calculated by treating the lens as an inflated torus. (For interpretation of the references to colour in this figure legend, the reader is referred to the web version of this article.)

chamber for measurements described below. Lenses were extracted from the eyes with minimal manipulation in this way without any vitreous attached. Lenses damaged during the dissections were not analyzed further. Extracted lenses were placed vertically oriented on a specially designed lens stand in a saline filled chamber and photographed in profile against a black background under a dissecting microscope (Olympus SZX12, Tokyo, Japan) with a 640 × 480 pixel digital video camera. Three images were captured
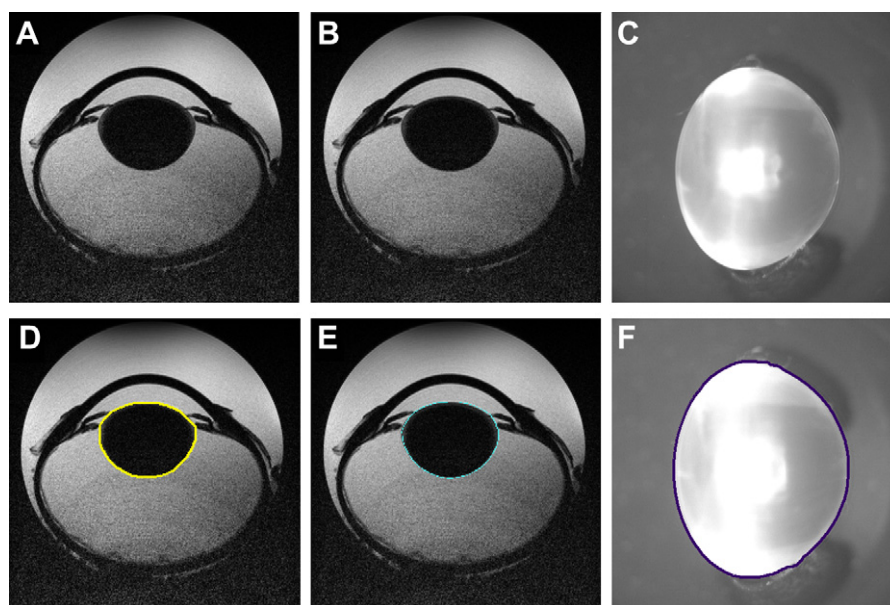

Fig. 2. Images of the lens from the same pig eye showing: (A) the most central slice from a stack of MR images, (B) the true central gray-scale interpolated image from the same 3-D stack of MR images, and (C) a profile image of the extracted lens after removal of the lens from the eye. Overlays show the lens edge overlays from volume calculations from these three images, respectively derived from (D) Method 2.3.1.1 on an MRI 2-D slice, (E) Method 2.3.2 applied to the whole MRI 3D stack, and (F) Method 2.4.1.1 applied to the extracted lens profile image.
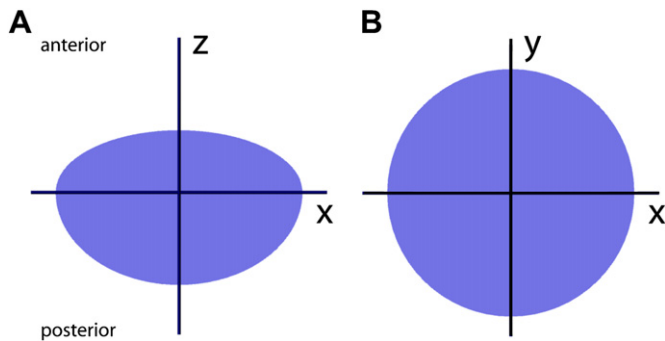
Fig. 3. Drawing shows the coordinate system used throughout this manuscript. (A) The lens in sagittal section showing the z-x plane. (B) The lens in equatorial section showing the x-y plane.

by positioning the lens on the stand, capturing an image, knocking the lens off the stand, replacing it again and capturing another image. This provided three independent images for analysis. The lens images were calibrated to millimeters by photographing millimeter ruled graph paper in the chamber at the same plane of focus as the lens equator.

2.2. Magnetic resonance imaging

MRI scans were performed on the intact pig eyes with a 7 T Biospec USR 70/30 horizontal bore with gradient insert BGA12 (Bruker, Karlsruhe, Germany) using a linear volume transmitter coil (72 mm inner diameter, Bruker, Germany) and a quadrature surface receiver coil (25 mm diameter, Bruker, Germany). The conical tube was placed into the bore such that the anterior–posterior axis of the eye was roughly vertical in raw MR images. The precise orientation of the eye was purposefully not controlled when the eye was glued in the tube or when the tube was positioned in the magnet. The actual optical axis of an enucleated pig eye is likely impossible to determine and tilt of the lens was compensated for through the image analysis methods. An initial scout scan simultaneously acquired slices in the z-y (sagittal-vertical), z-x (sagittal-horizontal) and x-y (equatorial) planes for the purpose of defining the regions of interest for the subsequent scans. Images were obtained using 2D rapid acquisition and relaxation enhancement (RARE) factor 32, repetition time (TR) 18 s, echo time (TE) 13 ms, with a total scan time

of 14 min. The gradient strength was adjusted so the theoretical pixel size matched the real pixel size. Scans of phantoms indicated that the temperature increased approximately 3 °C due to RF heating during a full volume scan. Since MRI contrast is temperature dependent, an analysis was performed to determine if there was any change in signal to noise ratio in the lens from early slices to late slices in a full 3D scan. No systematic change in image contrast was observed. Slice thickness was 0.5 mm with no overlap or separation between slices. The first three eyes were scanned with fields of view of either 24 × 24 or 30 × 30. After this, the field of view was standardized to 32 × 32 mm for all subsequent eyes. The slice pixel matrix was 256 × 256 and pixel resolutions ranged from 0.09375 × 0.09375 × 0.5 to 0.125 × 0.125 × 0.5. This resulted in image stacks of the lens with 45–50 images of 256 × 256 pixels. Although each acquired image represents a tissue slice of 0.5 mm thickness, each image obviously only comprises a single pixel in depth in a 3D image stack. To generate a full 3D image stack of 256 × 256 × 256 voxels of the entire lens, there are effectively $(256-50)/49 = 4.204$ intervening or missing pixel planes between each actual acquired image. There are potentially many different ways in which this 'missing' information can be 'filled in' or distributed to create the full 3D image stack for volumetric calculations, each with different benefits and drawbacks which are addressed below.

Lens volumes were calculated using 9 different methods (Table 1). Image acquisition and analysis was performed with custom Matlab code (The MathWorks, Inc., Natick, MA; toolboxes used were Data Acquisition, Image Acquisition, and Image Processing). Six of these methods used the MR images, one method measured the volume directly from the extracted lens, and two methods used digital microscopic profile images of the extracted lenses. Analyses were performed in triplicate on MR images in those cases where user decisions could introduce variations.

2.3. MR image analysis

The following six methods were applied to the MR images.

2.3.1. Central MR slice

Volume calculations were applied on between 3 and 5 of the individual central MRI 2D slices. The single slice that yielded the largest lens volume was then assumed to represent the true mid-lens 2D slice image. For each volume calculation, the selected 2D

Table 1
Summary of lens volume calculation methods.

	Experimental Procedure	Image Type	Method of Pre-Processing	Method of Segmentation	Method of Extending to 3D	Calculation Method
2.3.1.1	MRI	Slice/Projection	Rotation, Gray-Scale Threshold	Binary edges	Assume axial symmetry	Pappus Centroid Theorem
2.3.1.2	MRI	Slice/Projection	Rotation, Gray-Scale Threshold	Binary edges	Assume axial symmetry	Sum of Disks Method
2.3.2	MRI	Full Stack	Rotation, Spherical Transform	Probabilistic Gradient edge selection, user correction	Gray-Scale Interpolation	Count Pixels/Voxels
2.3.3.1	MRI	Full Stack	None	Canny edge, user correction	Cartesian Interpolation, polynomial extrapolation	Count Pixels/Voxels
2.3.3.2	MRI	Slice/Projection	None	Canny edge, user correction	Cartesian Interpolation, assume axial symmetry	Pappus Centroid Theorem
2.3.3.3	MRI	Slice/Projection	None	Canny edge, user correction	Cartesian Interpolation, assume axial symmetry	Sum of Disks Method
2.4.1.1	Isolated lens	Slice/Projection	Rotation, Gray-Scale Threshold	Binary edges	Assume axial symmetry	Pappus Centroid Theorem
2.4.1.2	Isolated lens	Slice/Projection	Rotation, Gray-Scale Threshold	Binary edges	Assume axial symmetry	Sum of Disks Method
2.4.2	Isolated lens	Calculate volume of fluid displaced by the lens				Mass of Displaced Fluid

cross sectional image in the z-x plane was converted to a binary image by setting a gray-scale threshold which differentiated the lens from background. Using this binary lens image, the orientation of the major axis of the lens relative to the horizontal axis of the image was calculated using the *regionprops* function in Matlab. This major axis was used to rotate the image so the largest diameter of the lens was aligned vertically with respect to the image borders. This vertically aligned binary image was then analyzed using either Pappus' Theorem or the Sum of Disks method as described below.

2.3.1.1. Pappus' theorem applied to central slice. After the lens image was rotated as described above, first the lens diameter was determined in pixels. The horizontal perpendicular bisector of the lens (lens axial thickness) was determined as the most central pixel row. This number was rounded up if it was an even number. This horizontal bisector does not necessarily result in an equal number of pixels in the upper and lower halves of the lens image, so in addition to using this central pixel row, another bisector one pixel above this and another one pixel below this were also determined. Of these three bisectors, the one that minimized the difference in the number of pixels between the upper and lower halves of the lens was selected as the vertical center of the lens. The centers of mass (centroids) for the upper and lower halves of the lens were calculated as the mean of all pixel image coordinates within each lens half. Lens volume was calculated using Pappus's second centroid theorem:

Volume of lens $=$ CSA $\times \pi \times$ d

where CSA is the average cross sectional area of the upper and lower halves of the lens image, π is the constant PI, and d is the vertical distance between the centroids of each half of the lens.(Gerometta et al., 2007) There is an inherent error in this method in that it assumes that the horizontal perpendicular bisector described above divides the lens equally into an upper and lower half each with exactly the same number of pixels. To determine the error introduced into the volume calculation from this assumption, lens volumes were calculated using the three different horizontal bisectors described above.

2.3.1.2. Sum of disks method applied to central slice. This analysis was performed on the same vertically aligned binary image that was created in Section 2.3.1 and using the same horizontal bisector chosen above. This method assumes that the lens is rotationally symmetric about the horizontal axis chosen and that the vertical alignment of the image is accurate. Given these two assumptions, each column of lens pixels in the binary image were taken to be a 2D representation of a disk with a thickness equal to one pixel and a diameter equal to the number of lens pixels in the column. The lens volume was calculated as the sum of the number of pixels in all the disks.

2.3.2. Spherical transform of the image stack

Lens volumes were calculated from entire MRI 3D stacks using gray-scale interpolation. The 256×256 pixel $\times 50$ image stack was interpolated by gray-scale cubic interpolation to a $256 \times 256 \times 256$ stack and then the major axis rotated in a similar manner as described above in Section 2.3.1 in two orthogonal planes to correct for tilt of the lens. The interpolated, rotated 3D stack of images was then transformed from Cartesian ($x =$ width, $y =$ depth, and $z =$ height) into spherical coordinates ($r =$ radius, $\theta =$ azimuth, and $\varphi =$ elevation) about a user selected position near the middle of the lens to generate a new stack of $76 \times 181 \times 360$ images. The middle of the lens selected by the user only needed to be approximate since variations would simply result in the edges of the lens being located in slightly different places in the transformed images but

would not affect the dimensions of the lens. The purpose of this spherical transformation was to render the curved lens surfaces more planar. If the lens were a sphere, the lens surfaces would appear as flat planes in the transformed images. The spherical transform facilitates the edge detection and identification of these surfaces. The spherical data was organized as a stack of depth, φ, with the size of each image being r by θ (Fig. 4). The position of the lens edge at each θ (horizontal row) was determined by taking the derivative of the image in the radial direction (vertical column). Lens surface edge positions were accumulated in a φ by θ image where the value of each pixel was the radius from the original point selected as the center of the lens at that $\varphi-\theta$ coordinate. Convolution of the φ by θ image with a Gaussian filter removed small, noisy variations in the surface radius in this image. All voxels in the Cartesian space which fell on or included the r, φ, θ edge
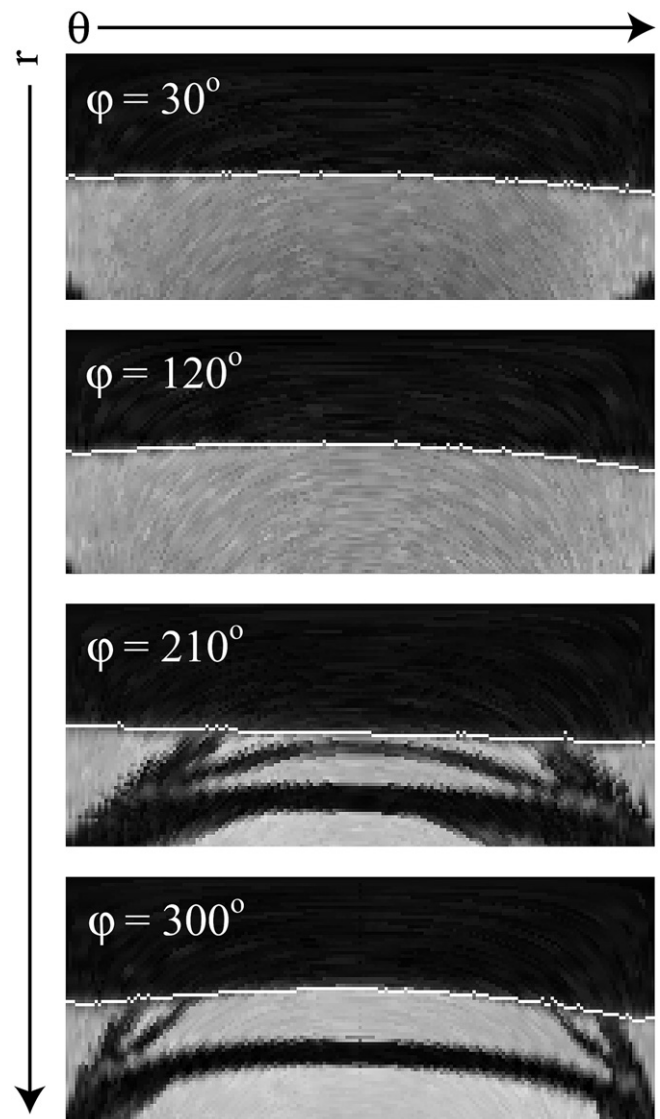

Fig. 4. Sample images from the spherical transform method (Method 2.3.2). The interpolated $256 \times 256 \times 256$ MRI stack has been spherically transformed into a $76 \times 181 \times 360$ stack defined by the spherical coordinates, r, θ, and φ, respectively. Lens edges were found using the stack of $r \times \theta$ images. Four of the sequence of 360 images are shown with detected lens edges marked in white and the value of φ for each image labeled in the corner. The upper darker region of each of these transformed images is the lens. The boundary between the lens and the anterior chamber, iris and vitreous chamber can be readily discerned as the edge marked in white.

coordinates were collected in a binary image stack. Lens volumes were calculated as a sum of all voxels included in this 3D binary stack.

2.3.3. Cartesian interpolation of the image stack

Lens volumes were calculated from entire MRI 3D stacks via interpolation of the lens surface Cartesian coordinates (x, y, z). The lens surface in each 2D image in the stack was found using a Canny edge detector with threshold values set automatically by the Matlab *edge* function. Pixels detected by the Canny edge detection algorithm which were not part of the lens surface (iris, for example) were manually removed. Lens surface data was interpolated in the direction of the stack depth (y) to the same pixel resolution as the in-plane (z-x) pixel resolution of each image slice using the Matlab *griddata* function with the method set to 'linear' which performs linear interpolation using Delaunay triangulation (Fig. 5). This interpolates the lens edge points in the spaces between acquired MRI slices (Fig. 5C and D), but does not extrapolate to the extreme equatorial edge of the lens where y is a minimum or a maximum. The reason the interpolation fails at the lens extremes is because there is, of course, no 2D MR image with a single pixel that represents the extreme edge points of the lens that would be required for successful interpolation to these points. As the image

slices near the edges of the lens, these single 2D MR images represent a 0.5 mm thick tissue slice from a region of the lens that is transitioning very steeply toward an apex. These single image slices therefore contain a section of the lens that is of considerably greater 'surface area' on what would be 'one side' of the image relative to the 'surface area' on what would be the 'other side' of the same image. This is analogous to the last slice of a loaf of Italian bread that contains the crust. To find the appropriate edge points of the lens, lens surface data from the 5 to 7 image slices nearest the lens edge were extrapolated by fitting a 5th order, 3-dimensional polynomial (Fig. 5E and F). All of the calculated lens surface points were then used to create a 3D binary image stack of the lens. This stack of lens surface points was rotated in two orthogonal dimensions to correct for tilt of the images. A 2D projection of the 3D image was calculated by collecting all x, z coordinates in the stack into a single binary image by setting each pixel y coordinate to zero. This effectively represents a profile image of the lens at the largest lens mid-plane section.

2.3.3.1. Sum of voxels.
Lens volumes were calculated as a sum of all voxels included in the 3D binary stack described in Section 2.3.3.

2.3.3.2. Pappus's theorem applied to projected 2D image.
Lens volume was calculated from the projected 2D image described at the end of Section 2.3.3 using Pappus's second centroid theorem as described in Section 2.3.1.1. This method was used to determine how accurately Pappus's second centroid theorem reproduces the 'true' lens volume effectively determined from the same set of data.

2.3.3.3. Sum of disks method applied to projected 2D image.
The sum of disks method described in Section 2.3.1.2 was used to calculate volume from the 2D image which was projected from the Cartesian interpolated stack described at the end of Section 2.3.3.

2.4. Extracted lens measurements

The following three methods were applied to the lenses after they were extracted from the eye.

2.4.1. Lens profile images
Lens volumes were calculated from the digitized lens profile images using a custom Matlab program which converted a gray-scale image to a binary image using a threshold to determine which pixels were included in the lens. The binary lens image was then rotated to ensure the major axis was vertically oriented.

2.4.1.1. Pappus' theorem applied to lens profile images.
Lens volumes were calculated from the binary lens profile image using Pappus's second centroid theorem as described in Section 2.3.1.1.

2.4.1.2. Sum of disks method applied to lens profile images.
Lens volumes were calculated from the binary lens profile image using the sum of disks method as described in Section 2.3.1.2.

2.4.2. Fluid displacement for volume determination
The actual volumes of the extracted lenses were measured using a fluid displacement method. Extracted lenses were placed on a 23 gauge wire ring holder and submerged, while still suspended on the wire ring, in a saline filled beaker on a laboratory scale to measure the mass of the saline solution displaced by the lens and wire holder. The wire holder was separately submerged to the same depth as before to determine the volume of fluid displaced by the wire alone and this value was subtracted from the weight of the fluid displaced by the lens and wire holder to provide the mass of the fluid displaced by the lens alone. The fluid density was assumed
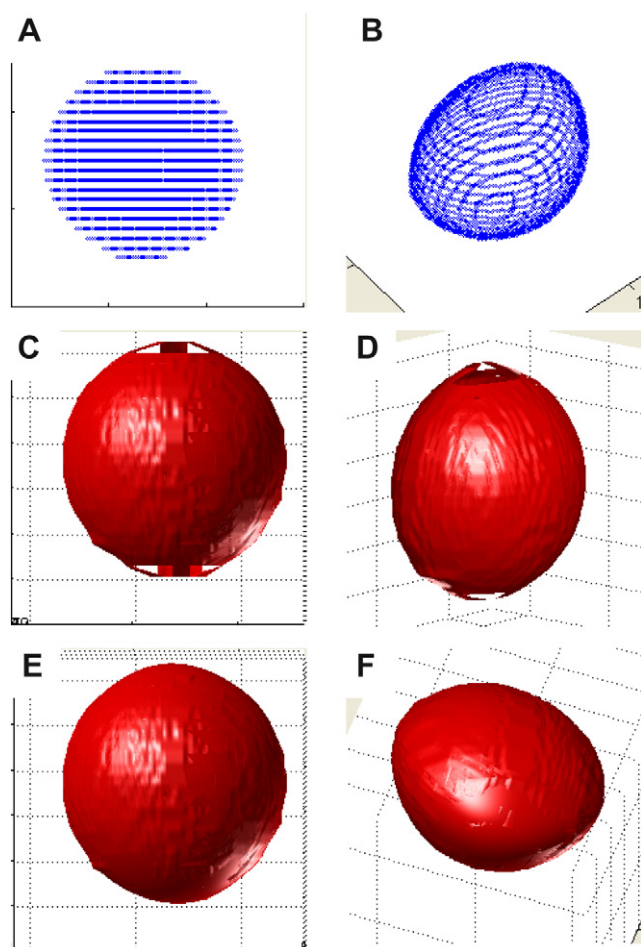

Fig. 5. Interpolation and extrapolation of lens edges from Method 2.3.3.1. Edges found using the Canny edge detector are shown (A) in the x-y view and (B) in a 3D xyz view. Interpolation of these edges fills in the spaces between slices as shown (C) in the x-y view and (D) in a 3D xyz view. Lens edges were extrapolated with a 5th order polynomial to fill in the two y-ends of the lens as shown (E) in the x-y view and (F) in a 3D xyz view.

to be 1.0 g/cm^3 and the volume of the lens is therefore directly proportional to the mass of fluid that the lens displaced. This method was calibrated using acrylic ball bearings of known diameter (Fig. 6).

2.5. Isotropic voxel and repeatability evaluation

On one eye, rather than using cyanoacrylate to glue the eye to the wall of the 50 ml conical tube, the eye was gently packed in gauze in the saline filled tube. This prevented eye movement, but allowed the eye to be removed and repositioned in the tube. First, a 3D isotropic MRI scan was performed with voxels of size 0.145 × 0.145 × 0.145 mm, FoV 32 × 32 × 32 mm, matrix 220 × 220 × 220, RARE factor 32, effective echo time 139 ms, repetition time 1200 ms, 1 average, scan time 22 min. Then, to assess repeatability, the eye was also scanned three times using the anisotropic MRI protocol described above. The eye was not moved between the isotropic scan and the first anisotropic scan. After each anisotropic scan, the eye was removed and then repositioned to ensure the scans could be considered to be independent. The images from the isotropic and the three repeated anisotropic scans were analyzed using the sum of voxels from the Cartesian interpolation method, 2.3.3.1, and the spherical transform method, 2.3.2.

3. Results

The lens volumes calculated from the three repeated anisotropic MRI scans and from the isotropic voxel scan are shown in Table 2. Each image stack was analyzed three times to account for user input in the analysis such as Canny edge selection or lens middle selection. The standard deviations for all analyses and all image stacks are 1.74 μl for the Cartesian interpolation method and 2.45 μl for the spherical transform method. The volume calculated from the isotropic scan and the first anisotropic scan (without moving the eye) differed by 5.19 μl for the Cartesian interpolation method and 4.35 μl for the spherical transform method.

Lens volume measured with Method 2.4.2 (fluid displacement) was considered to be the gold standard for comparison with the lens volume calculated with the image analysis methods. The average volume of all lenses from Method 2.4.2, (fluid displacement (Table 3)) was closest to the average volume calculated using Method 2.4.1.1 (Pappus from profile image), with a difference of 0.6%. The largest percentage difference of any of the methods
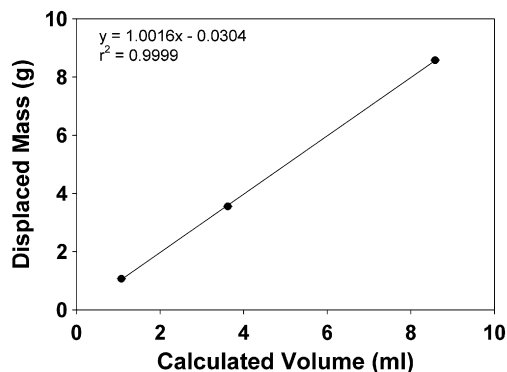
Table 2
Volume of one pig lens calculated from one isotropic and three anisotropic image stacks acquired from repeated MRI scans of the same pig eye. The isotropic stack and the first anisotropic stack were acquired with the eye in the same position. The eye was purposefully moved between the anisotropic scans.

Scan	3D Cartesian Interpolation	Spherical Transform
1 (isotropic)	390.99 ± 0.18	391.80 ± 0.40
1	396.18 ± 0.67	396.15 ± 0.35
2	392.46 ± 0.70	392.78 ± 0.52
3	393.46 ± 0.26	390.83 ± 1.34
Anisotropic Mean ± SD	394.03 ± 1.74	393.26 ± 2.45

evaluated from the average volume of Method 2.4.2 (fluid displacement) was 6.4% for Method 2.3.3.2 (Pappus from projected 2D MR image).

Variance in lens volumes could not be calculated from Methods 2.3.1.1 (Pappus from central MR slice) and 2.3.1.2 (Sum of disks from central slice) since there was only one image on which to perform analysis (the slice with the largest cross sectional area) and no user input that could introduce variability. As a result, these methods were compared to Method 2.4.2 (fluid displacement) using linear regressions rather than orthogonal regressions which require a measure of variance. All other volumetric methods were compared to Method 2.4.2 (fluid displacement) using orthogonal regressions. The relationships between lens volumes calculated from each image analysis method and Method 2.4.2 (fluid displacement) are shown in Fig. 7. The one-to-one line fell within the confidence limits of all methods in the range of the lens volumes. The MRI methods (Methods 2.3) of calculating volume showed higher correlations with Method 2.4.2 (fluid displacement) volumes, than did the profile image methods (Methods 2.4.1) as indicated by the R^2 values. Among the MRI methods, those derived from Cartesian interpolation (Methods 2.3.3) had higher correlations than those which selected the slice with the largest cross sectional area (Methods 2.3.1) or Method 2.3.2 (spherical transform) which used gray scale interpolation.

Pappus' method requires that the lens is divided in half. The shapes, sizes and cross sectional areas of these halves vary depending on image type and segmentation method. To determine the best horizontal dividing line between these halves, lens volumes were calculated for each of the three central horizontal dividing lines for each lens. The difference in the volumes calculated from the three central dividing lines provides a measure of one source of error inherent in Pappus' method. In Method 2.3.3.2, where the Pappus theorem was applied to the projected MRI slice of the Cartesian interpolated stack, the average inherent error in volume for all lenses was 3.17 μl ± 1.6 with a range of 0.18–7.56 μl.

Fig. 6. Calibration of the fluid displacement method for measuring lens volume using three acrylic ball bearings of known diameters. The volume of each ball was measured 5 times using the fluid displacement method. The standard deviations ranged from 0.0017 g to 0.0041 g. Error bars showing standard deviations are on the graph, but are smaller than the symbols. The regression line shows a slope near one and an intercept near zero.

Table 3
Average volumes for all the lenses for the different methods.

| Method Number	Method Description	Number of Lenses	Average Volume (μl)	% of Fluid Displacement
2.3.1.1	MRI slice (Pappus)	19	387.3 ± 41.8	98.7
2.3.1.2	MRI slice (Sum of Disks)	19	377.4 ± 41.4	96.2
2.3.2	MRI stack (spherical)	19	397.4 ± 37.3	101.3
2.3.3.1	MRI stack (Cartesian)	19	402.6 ± 38.9	102.6
2.3.3.2	MRI re-slice (Pappus)	19	417.3 ± 43.2	106.4
2.3.3.3	MRI re-slice (Sum of Disks)	19	407.0 ± 42.7	103.7
2.4.1.1	Profile image (Pappus)	18	389.8 ± 41.4	99.4
2.4.1.2	Profile image (Sum of Disks)	18	387.2 ± 41.2	98.7
2.4.2	Fluid Displacement	19	392.3 ± 38.6	100.0
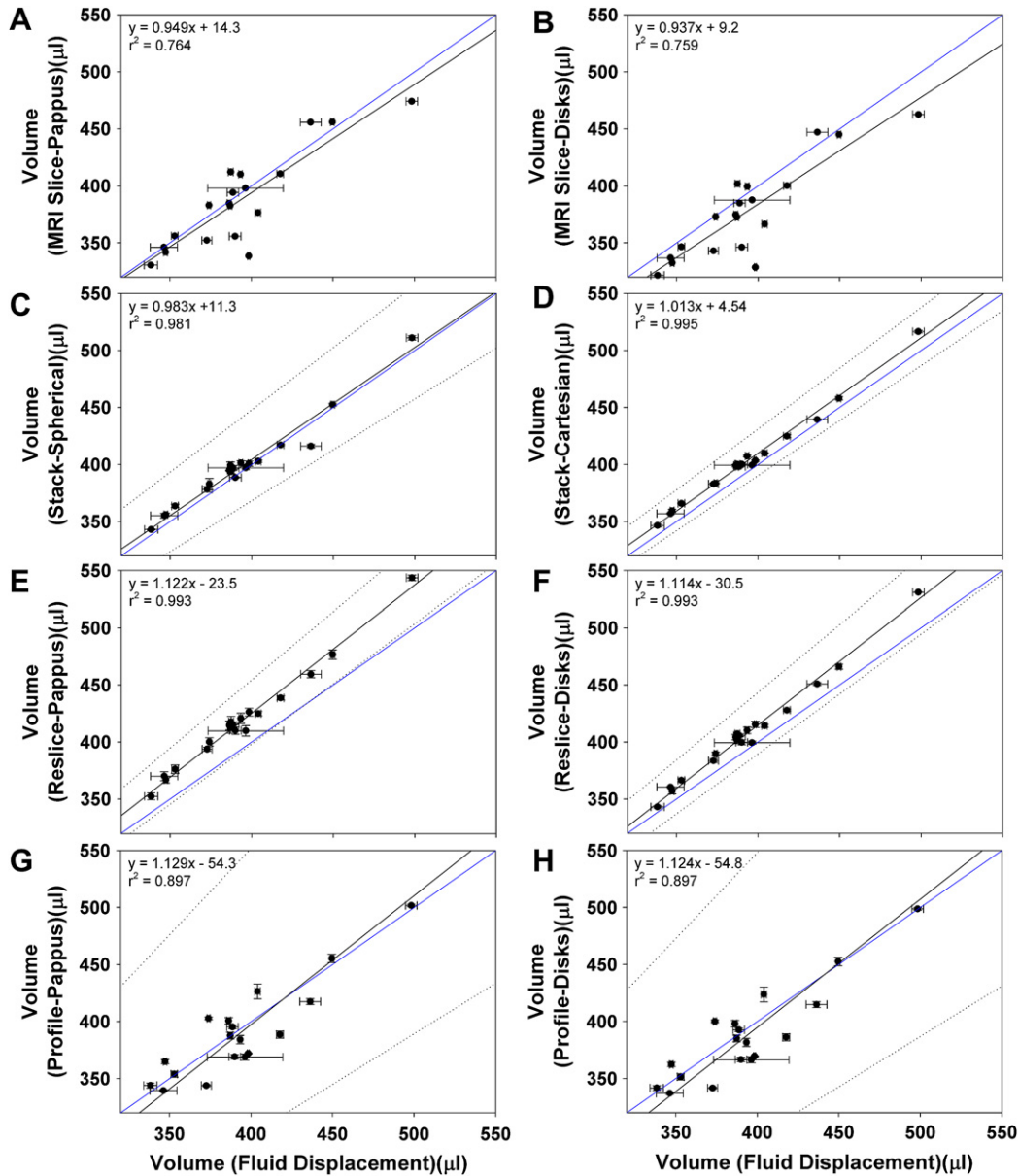
Fig. 7. Plots of lens volumes derived from (A) Method 2.3.1.1, application of Pappus's theorem to the central MRI 2-D slice, (B) Method 2.3.1.2, application of the sum of disks method to the central MRI 2-D slice, (C) Method 2.3.2, a spherical transform of the MRI 3-D stack, (D) Method 2.3.3.1, a Cartesian interpolation of the MRI 3-D stack, (E) Method 2.3.3.2, application of Pappus's theorem to the central slice calculated from the Cartesian interpolation of the MRI 3-D stack, (F) Method 2.3.3.3, application of the sum of disks method to the central slice calculated from the Cartesian interpolation of the MRI 3D Stack, (G) Method 2.4.1.1, application of Pappus's theorem to the extracted lens profile, (H) Method 2.4.1.2, application of the sum of disks method to the extracted lens profile image plotted against measured lens volumes from the fluid displacement method. Methods 2.3.1.1 and 2.3.1.2 show linear regression fits to the data because no standard deviations were available for each measurement. The rest show orthogonal regression fits to the data. Dashed lines indicate upper and lower confidence limits. The ideal one-to-one line is shown in blue. (For interpretation of the references to colour in this figure legend, the reader is referred to the web version of this article.)

The mean error of 3.17 μl was greater than the average standard deviation of the lens volumes obtained from the three individually captured profile images of the same lens (1.65 μl). In other words, capturing three individual profile images of the same lens gives a smaller variance than the variance due to one source of error in Pappus' method when applied to MR images. In Method 2.4.1.1 (Pappus from lens profile images), the average inherent error in the method (determined in the same way described above) was 0.88μl ± 0.70 with a range of 0.00–2.61 μl compared to an average standard deviation of lens volumes calculated from the three individually captured profile images of 2.39 μl.

4. Discussion

The fluid displacement method was considered as the gold standard. Fluid displacement volumes showed low variance within individual lenses in that the average of the standard deviations from the three measurements of each lens expressed as a percentage of each mean measurement from all lenses was 0.95%. Accuracy was determined for the volumetric measurements by using the same method on ball bearings of known volumes (Fig. 6).

A comparison was made between lens thicknesses calculated from the Cartesian interpolated stack (Method 2.3.3.1) and the
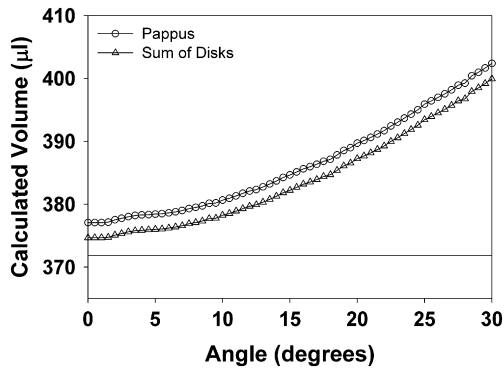
Fig. 8. Error in the volume calculated from the 2D projected images of a 3D simulated lens that was systematically tilted in the y-z plane. The solid horizontal line indicates the actual volume in calibrated units of the simulated 3D lens.

extracted lens profile image (Methods 2.4.1). Using Bland-Altman analysis, the average difference between lens thicknesses from these two methods was close to zero at −0.02 mm. The upper and lower confidence limits (2 × SD) were 0.20 mm and −0.23 respectively. From these data, it appears that there was no consistent difference in lens thickness when comparing the MR images and the extracted lens after dissection. This would indicate that the lens did not change shape in any consistent manner during removal from the eye.

The Pappus and sum of disks methods applied to the MRI central slice (Methods 2.3.1) and the two methods applied to profile images of the extracted lens (Methods 2.4.1) calculate lens volume from a single 2D image. These methods provided less precise volume estimates than the other image analysis methods. The R^2 values comparing these image analysis methods (Methods 2.3.1 and 2.4.1) with fluid displacement measured volumes ranged from 0.759–0.828. Various factors may contribute to this range of R^2 values, such as subjective judgments of the tilt of the lens prior to capturing the lens profile image (Methods 2.4.1). Unaltered MRI slices from Methods 2.3.1 (selected slice with the largest cross sectional area) may have a similar error due to eyes placed in the magnet in a tilted position. Although care was taken to ensure lenses were not tilted in the y-z plane for the lens profile images, the amount of lens tilt that might have been present was not measured and could not be corrected for. Lens tilt was corrected in the MRI data for the spherical transformed stack method (Method 2.3.2). In this method, the largest rotation required for any of the MR images was 15°. To determine the error from the lens profile images that a lens tilt in the y-z plane would introduce, the volume of a simulated 3D lens which was tilted at 0.5° increments from 0° to 30° was calculated using Pappus theorem and sum of disks (Fig. 8). The simulation shows that 15° of uncorrected tilt would

account for an error in volume of approximately 2.0%. The RMS percent differences between the fluid displacement measured volumes and the lens profile calculated lens volumes are 4.4% and 4.8% (Table 4). Since these differences are greater than 2.0%, they cannot be accounted for entirely by tilt. Further, the standard deviations for independent profile images of the same lens had an average of 0.6% ± 0.3% with a range of 0.1%–1.5%. It would be expected that the lens would be tilted differently in each image, yet this range of standard deviations is lower than either the 2.0% predicted for lens tilt or the actual RMS percent differences between the fluid displacement measured volumes and the lens profile calculated lens volumes.

Methods using the central MRI slice (Method 2.3.1) and the lens profile images (Methods 2.4.1) use gray-scale thresholding which requires user input and is subject to variations. To determine the effect of the choice of threshold, two profile images were tested over the widest range of subjectively reasonable threshold values determined by one user (MW). The calculated volume using the Pappus method changed 1.7% over a threshold range of 25 (over a possible range of 0−255) and by 1.9% over a threshold range of 33. Therefore, the largest differences in lens volume from the gold standard also cannot be explained solely by the threshold.

The selection of the MRI slice or plane of focus of the captured image to be analyzed could contribute to the reduced precision of the strictly 2D methods. Since the MRI slice dimensions (slice thickness, number of slices) in Methods 2.3.1 (central MRI slice) were pre-set as parameters during the MRI scans, the methods using the central MRI slice (Methods 2.3.1) might be expected to show greater precision than the lens image profile methods (Methods 2.4.1). However, the limited resolution in the MRI stack depth (slices taken at every 0.5 mm) could have a similar type of error to the error introduced by the microscope plane of focus in the digitally captured profile images. If the MR image section with the largest cross sectional area was not actually a true mid-lens sagittal section through the lens, the lens volume would be underestimated. In the case of MRI, thicker image slices will underestimate volume because the lens edges seen in the MR images are effectively an average lens edge within this entire slice thickness. The lens edge at the true center of the lens with the largest circumference would appear smaller from this averaging. The effect of this error would be even greater in previous studies where 3 mm slices were analyzed (Atchison et al., 2008; Jones et al., 2007; Kasthurirangan et al., 2011; Strenk et al., 1999, 2004). The true center of the lens is also unlikely to be exactly centered within the central MR image slice thickness resulting in stronger influence on the lens edge from one side of the lens than the other, which would also underestimate the true volume. All these sources of error on the central MR image would underestimate the true lens volume, and this is in fact what is observed (Table 4). For the lens profile images, an improperly focused image could either

Table 4
Comparisons between the fluid displacement measured lens volumes and the volumes calculated from the different imaging methods.

	Method	Mean difference between imaging method and measured lens volumes (mean ± SD)	Mean % relative to measured lens volumes	RMS difference between imaging method and measured lens volumes	RMS % relative to measured lens volumes
2.3.1.1	MRI slice (Pappus)	−5.65μl ± 20.44	−1.4%	20.68 μl	5.3%
2.3.1.2	MRI slice (Sum of Disks)	−15.55μl ± 20.47	−4.0%	25.27 μl	6.4%
2.3.2	MRI stack (spherical)	4.48μl ± 7.43	1.1%	8.51 μl	2.2%
2.3.3.1	MRI stack (Cartesian)	10.38μl ± 3.69	2.6%	10.98 μl	2.8%
2.3.3.2	MRI re-slice (Pappus)	25.07μl ± 6.25	6.4%	25.79 μl	6.6%
2.3.3.3	MRI re-slice (Sum of Disks)	14.14μl ± 6.29	3.6%	15.40 μl	3.9%
2.4.1.1	Profile image (Pappus)	−2.75μl ± 17.66	−0.7%	17.39 μl	4.4%
2.4.1.2	Profile image (Sum of Disks)	−5.99μl ± 18.40	−1.5%	18.86 μl	4.8%

underestimate or overestimate the actual lens volume. Table 4 shows that the lens profile image analysis methods underestimate true lens volume. This could also be due to calibration inaccuracies.

The spherical transform of MR image stack (Method 2.3.2) has the advantages that the entire stack was used in the volume calculation and no equation is required to model the lens surfaces. The main sources of error may come from the gray-scale interpolation of the slices to a 3D stack and the required smoothing, both of which convert the transformed data to an inexact and somewhat idealized reproduction of the original data. However, the interpolation uses neighboring slices so multiple images contribute to the segmentation process.

The Cartesian interpolated stack (Methods 2.3.3), also used the full MRI stack to calculate volume. These methods did not use any image smoothing, gray-scale interpolation, or other pre-processing or a model for calculations. Therefore, although these methods have the necessary disadvantage of segmentation prior to interpolation, they had the advantage of better interpolation based on surface position rather than gray-scale intensity. The Pappus' method and the sum of disks applied to the 2D projected MRI image (Methods 2.3.3.2 and 2.3.3.3) required the additional step of calculating a 2D projected image. All three of these methods (Methods 2.3.3.1, 2.3.3.2 and 2.3.3.3) showed superior precision compared to the fluid displacement measured volumes relative to the other image analysis methods as indicated by R^2 values of approximately 0.99 with the R^2 value from summing voxels from the 3D stack (Method 2.3.3.1) being fractionally higher. This latter method was also the most accurate method having a slope of the linear regression with fluid displacement measured lens volumes closest to 1.0 (Table 5) and the smallest standard deviations (Table 4). All three methods provided results which were close to, but consistently overestimated, the fluid displacement measured lens volume. The most likely cause of overestimation is the segmentation, which in this case was the Canny edge detector. The Matlab default threshold value was used for the Canny edge detector. It is likely that changing this value would affect the estimation of the lens volumes.

The accuracy and precision of the image analysis methods are evident in the root-mean-square (RMS) difference between volumes calculated by the image analysis methods and the fluid displacement measured volumes (Table 4). The most accurate lens volumetric calculations require analysis of full 3D stacks of MR images, but this still results in an error of 8.51 μl, which is the volume of a 2.04 × 2.04 × 2.04 mm cube (Fig. 9).

Rosen et al. (Rosen et al., 2006) applied an ellipsoidal fit to the Strenk et al. human lens MRI surfaces (Strenk et al., 1999, 2004) and found a range of volumes of human lenses from 130 to 200 μl over an age range of 20–62 years. Similarly, Koretz et al. (Koretz et al., 2001) showed an increase in lens volume over the age range of 18–70 years from 200 to 260 μl assuming their data should be multiplied by a factor of 1000 (Hermans et al., 2009). These 60 and
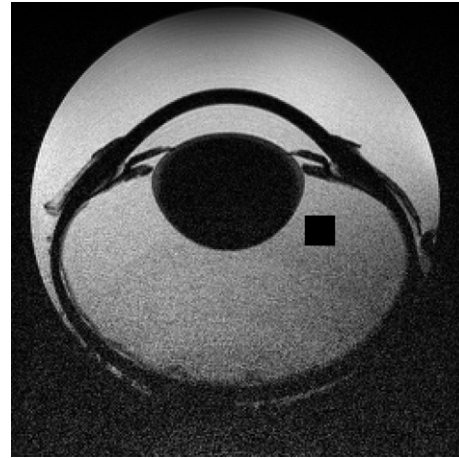

Fig. 9. Demonstration of the extent of error in the measured volumes drawn into the central slice of a stack of pig lens MR images. The black square adjacent to the lens represents a cube with sides of length 2.04 mm. This is the 2D equivalent of an error in the lens volume of 8.51 μl which is the same as the RMS of the differences in volume between Method 2.3.2 (spherical transform of the image stack) and fluid displacement measured lens volumes. This lens had a fluid displacement measured volume of 389 μl.

70 μl age-related increases in MRI calculated human lens volume are greater than the minimum error reported here for pig lenses which have considerably larger volumes than human lenses and therefore are certainly within the resolution limits of the methods described here.

Strenk et al. (Strenk et al., 2004) measured CSA of human lenses in MR images and reported an increase in CSA with accommodation and further stated that these increases in CSA should translate to increases in volume assuming symmetry about the lens anterior–posterior axis. Insufficient information was given by Strenk et al. to convert CSA to volume except for the two subjects in their repeatability study. In these two cases, an ellipsoidal fit can be applied to the data to give an estimate of the volume as was done by Rosen et al. (Rosen et al., 2006). The calculated volume of a 22-year-old lens increased with accommodation by 4.7 μl and the calculated volume of a 49-year-old lens remained at 180.4 μl. These values are less than the minimum error reported here for pig lenses (Method 2.3.3.1 – Cartesian interpolation). The method of Strenk et al. was most similar to Method 2.3.1.1 (Pappus on MRI slices) which had an RMS error of 20.68 μl. Therefore, the methods used by Strenk et al. would not have had the resolution necessary to detect the increase in lens volume reported. Hermans et al. reported a mean volume of human lenses of 160.1 ± 2.5 μl and a non-significant change in lens volume of 0.1 μl (mm³) with accommodation in five human subjects (Hermans et al., 2009). Using a photographic method of image acquisition, Zamudio et al. (Zamudio et al., 2008) reported that bovine lenses decrease in volume by an average of 72 μl (−10 μl–180 μl) when mechanically stretched. The method used

Table 5
Lens volume linear regression results for Methods 2.3.1.1 and 2.3.1.2 and orthogonal regression results for the other volumetric methods versus the fluid displacement measured lens volume.

Method	Method Description	Intercept	Slope	Lower Confidence Limit	Upper Confidence Limit	Correlation	R^2
2.3.1.1	MRI slice (Pappus)	14.3	0.949	NA	NA	NA	0.764
2.3.1.2	MRI slice (Sum of Disks)	9.2	0.937	NA	NA	NA	0.759
2.3.2	MRI stack (spherical)	11.28	0.983	0.892	1.091	0.981	0.963
2.3.3.1	MRI stack (Cartesian)	4.54	1.013	0.964	1.066	0.995	0.990
2.3.3.2	MRI re-slice (Pappus)	−23.46	1.122	1.054	1.195	0.993	0.985
2.3.3.3	MRI re-slice (Sum of Disks)	−30.47	1.114	1.050	1.185	0.993	0.986
2.4.1.1	Profile image (Pappus)	−54.33	1.129	0.887	1.514	0.897	0.804
2.4.1.2	Profile image (Sum of Disks)	−54.85	1.124	0.883	1.507	0.897	0.805

here that was most similar was Pappus's theorem applied to the profile image of the extracted lens (Method 2.4.1.1). This had an RMS error of 17.39 μl. Based on this, changes smaller than about 20 μl would be too small to detect. Sheppard et al. (Sheppard et al., in press) reported a 2.3% increase in volume in human lens with accommodation which corresponds to an increase in volume of 3.56 μl based on their reported average lens volume. This is less than the minimum error reported here for Cartesian interpolation. The increases in lens volume during accommodation that have been reported in the literature are therefore either close to or below the resolution limits of the methods being employed to measure lens volume. A question remains as to how lens volume could increase during accommodation. One potential caveat that has rarely been addressed in the published in vivo studies is how the iris is differentiated from the lens in the image analysis methods employed. As the eye accommodates, the iris constricts and so a larger part of the lens surface is in contact with the iris. Perhaps the increase in lens volume that has been reported is simply an artifact due to an inability to accurately differentiate iris from lens, and more so in the accommodated eye. Kasthurirangan et al. addressed the problem associated with contact between iris and lens by not analyzing portions of the lens in contact with the iris, however they did not report lens volume measurements. It is possible that the iris and lens could be distinguished by adjusting the T1 and T2 weighting of the scans. However, this still does not result in a clear lens surface as exists within the pupil or on the posterior lens surface where the iris is not present. Langner et al. showed MR images of excised human and monkey eyes where the iris intensity was noticeably different from the lens (Langner et al., 2010). However, the portions of the iris touching the lens would still create some challenges to image analysis.

None of the methods presented here used a model to represent the lens surface. Methods using models described previously were attempted (Hermans et al., 2009; Reilly and Ravi, 2010). In the method of Hermans et al., all surface points from human lenses were projected to one cross-sectional plane by setting the angular component to zero and then these points were fitted with an aspheric equation. This method worked poorly on pig lenses because of the constraints described for the aspheric equation. Other constraints to join the lens caps to the lens surfaces were attempted, but resulted in discontinuities so this method was not pursued further. The four models proposed by Reilly and Ravi for porcine lenses were also attempted. Visual inspection of fits showed that the equation poorly fit the data – especially at the anterior and posterior lens poles, so this method was not pursued further. Pappus's theorem or sum of disks applied to any of the 2D images or counts of voxels in either spherically transformed stacks or Cartesian interpolated stacks required the assumption of symmetry about the anterior–posterior axis. However, all these methods could be applied to primate lenses as they were applied here to porcine lenses.

The experimental MRI conditions used here on enucleated pig eyes have many advantages with respect to image resolution over most MRI methods that have previously been reported for use with living human subjects. The scanner used was a 7 T MRI with a small diameter bore for use with small animals. As has recently been demonstrated, 7 T allows for increased image resolution over magnet strengths that have generally been used (Langner et al., 2010; Richdale et al., 2009). Additionally, isolated pig eyes were used which were glued to the edge of a conical tube in saline and this ensured absolute stability of the eyes. In vivo MR imaging in living human eyes would result in reduced resolution and accuracy due to eye movements, blinks and the need for shorter imaging time. Even with efforts to avoid blinks (Sheppard et al., in press), complete ocular stability cannot be achieved. Regardless, the results reported here indicate that greater accuracy will result from analysis which utilizes data from the full 3D image stack as opposed to a single 2D central image slice. Even with the near ideal MR imaging methods employed here, accuracy of the lens volume of better than 1% is not reliably attainable. With the reduced image resolution that would result from imaging living human eyes, the accuracy will certainly decrease further. Therefore, if development of reliable A-IOLs requires greater accuracy in measuring lens volume, this will not be attainable with MRI methods published to date.

References

Atchison, D.A., Markwell, E.L., Kasthurirangan, S., Pope, J.M., Smith, G., Swann, P.G., 2008. Age-related changes in optical and biometric characteristics of emmetropic eyes. J. Vis. 8, 1–20.

Augusteyn, R.C., 2007. Growth of the human eye lens. Mol. Vis. 13, 252–257.

Baikoff, G., Lutun, E., Wei, J., Ferraz, C., 2004. Anterior chamber optical coherence tomography study of human natural accommodation in a 19-year-old albino. J. Cataract Refract. Surg. 30, 696–701.

Borja, D., Manns, F., Ho, A., Ziebarth, N.M., Acosta, A.C., Arrieta-Quintera, E., Augusteyn, R.C., Parel, J.M., 2010a. Refractive power and biometric properties of the nonhuman primate isolated crystalline lens. Invest. Ophthalmol. Vis. Sci. 51, 2118–2125.

Borja, D., Siedlecki, D., de Castro, A., Uhlhorn, S., Ortiz, S., Arrieta, E., Parel, J.M., Marcos, S., Manns, F., 2010b. Distortions of the posterior surface in optical coherence tomography images of the isolated crystalline lens: effect of the lens index gradient. Biomed. Opt. Express 1, 1331–1340.

Dubbelman, M., van der Heijde, G.L., 2001. The shape of the aging human lens: curvature, equivalent refractive index and the lens paradox. Vision Res. 41, 1867–1877.

Dubbelman, M., van der Heijde, G.L., Weeber, H.A., 2005. Change in shape of the aging human crystalline lens with accommodation. Vision Res. 45, 117–132.

Gerometta, R., Zamudio, A.C., Escobar, D.P., Candia, O.A., 2007. Volume change of the ocular lens during accommodation. Am. J. Physiol. Cell Physiol. 293, C797–C804.

Glasser, A., Campbell, M.C.W., 1999. Biometric, optical and physical changes in the isolated human crystalline lens with age in relation to presbyopia. Vision Res. 39, 1991–2015.

Glasser, A., Wendt, M., Ostrin, L., 2006. Accommodative changes in lens diameter in rhesus monkeys. Invest. Ophthalmol. Vis. Sci. 47, 278–286.

Grulkowski, I., Gora, M., Szkulmowski, M., Gorczynska, I., Szlag, D., Marcos, S., Kowalczyk, A., Wojtkowski, M., 2009. Anterior segment imaging with Spectral OCT system using a high-speed CMOS camera. Opt. Express 17, 4842–4858.

Hermans, E.A., Pouwels, P.J., Dubbelman, M., Kuijer, J.P., van der Heijde, R.G., Heethaar, R.M., 2009. Constant volume of the human lens and decrease in surface area of the capsular bag during accommodation: an MRI and Scheimpflug study. Invest. Ophthalmol. Vis. Sci. 50, 281–289.

Jones, C.E., Atchison, D.A., Pope, J.M., 2007. Changes in lens dimensions and refractive index with age and accommodation. Optom. Vis. Sci. 84, 990–995.

Kasthurirangan, S., Markwell, E.L., Atchison, D.A., Pope, J.M., 2011. MRI study of the changes in crystalline lens shape with accommodation and aging in humans. J. Vis. 11.

Kong, C.W., Gerometta, R., Alvarez, L.J., Candia, O.A., 2009. Changes in rabbit and cow lens shape and volume upon imposition of anisotonic conditions. Exp. Eye Res. 89, 469–478.

Koretz, J.F., Cook, C.A., Kaufman, P.L., 2001. Aging of the human lens: changes in lens shape at zero-diopter accommodation. J. Opt. Soc. Am. A Opt. Image Sci. Vis. 18, 265–272.

Langner, S., Martin, H., Terwee, T., Koopmans, S.A., Krüger, P.C., Hosten, N., Schmitz, K.P., Guthoff, R.F., Stachs, O., 2010. 7.1 T MRI to assess the anterior segment of the eye. Invest. Ophthalmol. Vis. Sci. 51, 6575–6581.

Marussich, L.K., Nankivil, D., Maceo, B.M., Arrieta, E., Urs, R., Manns, F., Ho, A., Augusteyn, R.C., Parel, J.M., 2011. Changes in primate crystalline lens volume during simulation of accommodation in a lens Stretcher. Invest. Ophthalmol. Vis. Sci. 52, 814.

Reilly, M.A., Ravi, N., 2010. A geometric model of ocular accommodation. Vision Res. 50, 330–336.

Richdale, K., Wassenaar, P., Teal, B.K., Abduljalil, A., Christoforidis, J.A., Lanz, T., Knopp, M.V., Schmalbrock, P., 2009. 7 Tesla MR imaging of the human eye in vivo. J. Magn. Reson. Imaging 30, 924–932.

Rosales, P., Dubbelman, M., Marcos, S., van der Heijde, R., 2006. Crystalline lens radii of curvature from Purkinje and Scheimpflug imaging. J. Vis. 6, 1057–1067.

Rosales, P., Marcos, S., 2006. Phakometry and lens tilt and decentration using a custom-developed Purkinje imaging apparatus: validation and measurements. J. Opt. Soc. Am. A Opt. Image Sci. Vis. 23, 509–520.

Rosen, A.M., Denham, D.B., Fernandez, V., Borja, D., Ho, A., Manns, F., Parel, J.M., Augusteyn, R.C., 2006. In vitro dimensions and curvatures of human lenses. Vision Res. 46, 1002–1009.

Shen, M., Wang, M.R., Yuan, Y., Chen, F., Karp, C.L., Yoo, S.H., Wang, J., 2010. SD-OCT with prolonged scan depth for imaging the anterior segment of the eye. Ophthalmic Surg. Lasers Imaging 41, S65–S69.

Sheppard, A.L., Evans, C.J., Singh, K.D., Wolffsohn, J.S., Dunne, M.C.M., Davies, L.N., . Three-dimensional magnetic resonance imaging of the phakic crystalline lens during accommodation. Investigative Ophthalmology & Visual Science, in press.

Strenk, S.A., Semmlow, J.L., Strenk, L.M., Munoz, P., Gronlund-Jacob, J., DeMarco, J.K., 1999. Age-related changes in human ciliary muscle and lens: a magnetic resonance imaging study. Invest. Ophthalmol. Vis. Sci. 40, 1162–1169.

Strenk, S.A., Strenk, L.M., Guo, S., 2006. Magnetic resonance imaging of aging, accommodating, phakic, and pseudophakic ciliary muscle diameters. J. Cataract Refract. Surg. 32, 1792–1798.

Strenk, S.A., Strenk, L.M., Semmlow, J.L., DeMarco, J.K., 2004. Magnetic resonance imaging study of the effects of age and accommodation on the human lens cross-sectional area. Invest. Ophthalmol. Vis. Sci. 45, 539–545.

Uhlhorn, S.R., Borja, D., Manns, F., Parel, J.M., 2008. Refractive index measurement of the isolated crystalline lens using optical coherence tomography. Vision Res. 48, 2732–2738.

Urs, R., Ho, A., Manns, F., Parel, J.M., 2010. Age-dependent Fourier model of the shape of the isolated ex vivo human crystalline lens. Vision Res. 50, 1041–1047.

Urs, R., Manns, F., Ho, A., Borja, D., Amelinckx, A., Smith, J., Jain, R., Augusteyn, R., Parel, J.M., 2009. Shape of the isolated ex-vivo human crystalline lens. Vision Res. 49, 74–83.

Wendt, M., Croft, M.A., McDonald, J., Kaufman, P.L., Glasser, A., 2008. Lens diameter and thickness as a function of age and pharmacologically stimulated accommodation in rhesus monkeys. Exp. Eye Res. 86, 746–752.

Wilson, R.S., 1997. Does the lens diameter increase or decrease during accommodation? Human accommodation studies: a new technique using infrared retro-illumination video photography and pixel unit measurements. Trans. Am. Ophthalmol. Soc. 95, 261–267.

Zamudio, A.C., Candia, O.A., Kong, C.W., Wu, B., Gerometta, R., 2008. Surface change of the mammalian lens during accommodation. Am. J. Physiol. Cell Physiol. 294, C1430–C1435.